

This is an Open Access document downloaded from ORCA, Cardiff University's institutional repository: <https://orca.cardiff.ac.uk/id/eprint/129541/>

This is the author's version of a work that was submitted to / accepted for publication.

Citation for final published version:

Wang, Haige, Hou, Bo , Yang, Yang, Chen, Qianwang, Zhu, Meifang, Thomas, Arne and Liao, Yaozu 2018. Cobalt nanocrystals encapsulated in heteroatom-rich porous carbons derived from conjugated microporous polymers for efficient electrocatalytic hydrogen evolution. *Small* 14 (42) , -. 10.1002/sml.201803232

Publishers page: <http://dx.doi.org/10.1002/sml.201803232>

Please note:

Changes made as a result of publishing processes such as copy-editing, formatting and page numbers may not be reflected in this version. For the definitive version of this publication, please refer to the published source. You are advised to consult the publisher's version if you wish to cite this paper.

This version is being made available in accordance with publisher policies. See <http://orca.cf.ac.uk/policies.html> for usage policies. Copyright and moral rights for publications made available in ORCA are retained by the copyright holders.



Cobalt Nanocrystals Encapsulated in Heteroatom-Rich Porous Carbons Derived from Conjugated Microporous Polymers for Efficient Electrocatalytic Hydrogen Evolution

1 Haige Wang¹, Bo Hou³, Yang Yang⁴, Qianwang Chen⁴, Meifang Zhu^{1,*}, Arne Thomas^{2,*}, Yaozu Liao^{1,2,*}

2 ¹State Key Laboratory for Modification of Chemical Fibers and Polymer Materials & College of
3 Materials Science and Engineering, Donghua University, Shanghai 201620, China

4 ²Department of Chemistry and Functional Materials, Technische Universität Berlin, Berlin 10623,
5 Germany

6 ³Department of Engineering Science, University of Oxford, OX1 3PJ, Oxford, U.K

7 ⁴Hefei National Laboratory for Physical Sciences at Microscale and Department of Materials Science &
8 Engineering, University of Science and Technology of China, Hefei, China

9 *Corresponding Author: yz.liao@dhu.edu.cn; arne.thomas@tu-berlin.de and zmf@dhu.edu.cn

12
13 **Enabling an efficient hydrogen evolution reaction (HER) using earth-abundant metal catalysts is**
14 **one of the most significant challenges in electrocatalysis. Cobalt nanocrystals encapsulated in**
15 **nitrogen and oxygen dual-doped porous carbon is such an efficient and stable electrocatalyst for**
16 **HER. Microporous, heteroatom-rich polymer networks, which are applied as carbon precursor**
17 **and metal support, can be deposited directly on carbon fiber cloth, removing the necessity of**
18 **using any binder for the preparation of the electrocatalyst. This electrocatalyst, with remarkably**
19 **low cobalt loading (1.35 wt%), achieves a Tafel slope of 46 mV dec⁻¹ and an overpotential of only**
20 **69 mV at a current density of 10 mA cm⁻² in 0.5 M sulfuric acid solution. Surface structural and**
21 **computational studies reveal that the superior behavior is owing to the decreased ΔG_{H^*} for HER.**

22
23 Electrocatalytic water splitting represents one of the most promising pathways to produce hydrogen as
24 a sustainable fuel.¹ The development of active electrocatalysts is crucial to promote the hydrogen and
25 oxygen evolution rate and reduce the overpotentials of these reactions. Platinum (Pt) supported on
26 activated carbons is currently the benchmark catalyst for the hydrogen evolution reaction (HER), but
27 has its drawbacks in scarcity and high-cost of the active compound.² In recent years, many research
28 efforts have been devoted to find non-noble metal compounds as possible alternatives for HER
29 catalysts. Earth-abundant transition metal (e.g. Co, Ni or Mo) compounds have been shown to be
30 promising catalytic materials for HER in alkaline electrolytes.^{3,4} Nevertheless, many of these
31 compounds are not stable in acidic media, needed for an efficient HER.⁵ Recently, transition metal-
32 based nanoparticles encapsulated in carbons have attracted considerable attentions to promote the HER
33 activity and stability.⁶⁻¹⁰ However, these materials are often prepared by complex multi-step syntheses,
34 again raising issues about cost and scalability. A facile synthesis of low-cost and acid-stable HER
35 catalysts would be therefore highly desirable.¹¹ Experimental and theoretical results have shown that
36 single or dual heteroatom doping of carbonaceous materials, with nitrogen, sulfur, phosphine or boron
37 can significantly improve the HER performance.¹²⁻¹⁵ Herein, we apply a conjugated microporous
38 polymer (CMP) as precursor for a unprecedented nitrogen (N) and oxygen (O) dual-doped carbon with
39 encapsulated metal (Co) nanoparticles, which indeed show superior performance as HER catalyst.

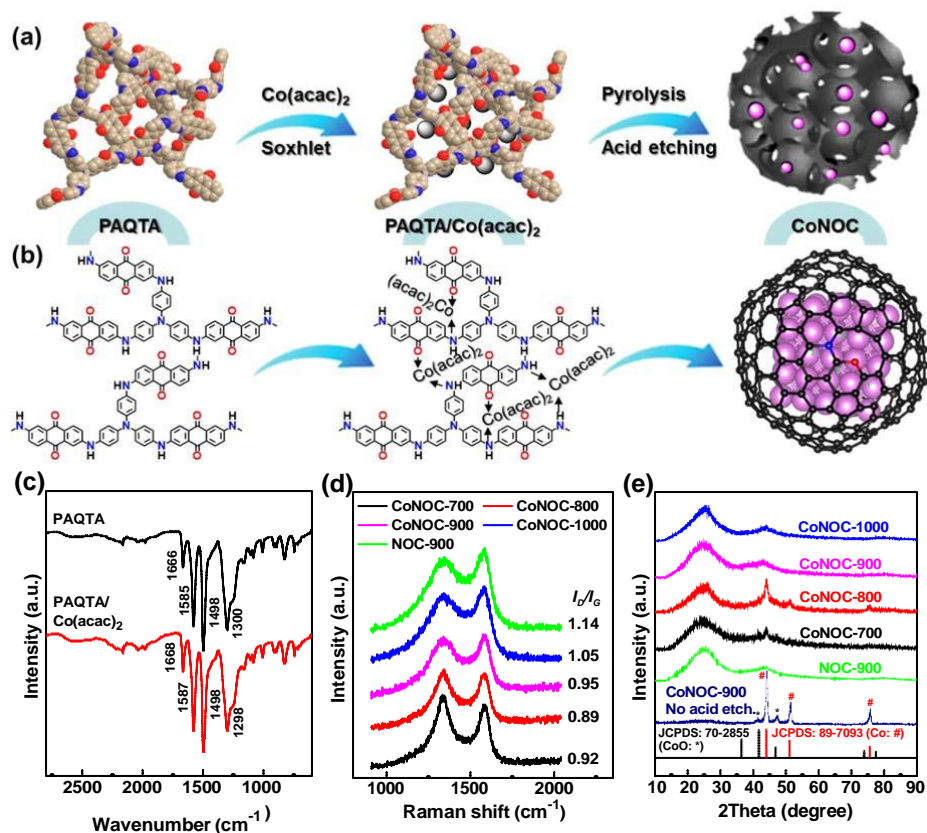
40 CMPs provide large specific surface areas and high chemical stability. These features make them
41 promising materials for gas uptake, catalysis, and energy storage applications.¹⁶ CMPs furthermore are
42 interesting materials for the rational design of heteroatom-doped porous carbon materials.¹⁷ We have
43 recently shown, that using the Buchwald-Hartwig coupling,¹⁸ N and O-rich (>20 wt%) CMPs with 2,6-

44 diaminoanthraquinonylamine (DAQ) and triphenylamine (TA) moities (i.e. PAQTA) can be easily
45 synthesized and perform excellent electrochemical energy storage performance. Owing to its cross-
46 linked network structure and intrinsic porosity as well as the high amount of heteroatoms, PAQTA
47 seems to be a promising support for metal nanoparticles and precursor for heteroatom-doped porous
48 carbon materials. We herein demonstrate a scalable and straightforward pyrolysis route to metallic
49 cobalt nanoparticles (CoNPs) encapsulated in N,O-dual doped carbons (CoNOCs) as HER catalysts
50 using PAQTA networks as precursors. The fabrication of binder-free membrane-like HER electrodes is
51 possible through the deposition of the catalysts on woven carbon fiber cloth (CFC). The high flexibility
52 of the resulting electrodes allows scaling-up the catalytic setup.

53 **Results**

54 **Preparation and characterization of CoNOCs.** The bulk CoNOC-x catalysts were prepared by
55 impregnating PAQTA with $\text{Co}(\text{acac})_2$ in a first step, followed by pyrolysis under N_2 atmosphere at four
56 temperatures (i.e. 700, 800, 900, and 1000 °C, x indicates the pyrolysis temperature) followed by
57 removal of weakly bound metal species by etching with aqueous sulfonic acid (Fig. 1a,b). where.
58 Metal-free carbon catalysts named NOC-x were prepared in absence of $\text{Co}(\text{acac})_2$ for comparison. The
59 Fourier-Transform Infrared (FT-IR) spectrum of $\text{Co}(\text{acac})_2$ impregnated PAQTA show a very similar
60 pattern to the pristine precursor (Fig. 1c).¹⁸ Raman spectra were measured to investigate the
61 graphitization of CoNOCs. All spectra show two peaks at 1585 and 1345 cm^{-1} associated with the D
62 and G bands (Fig. 2d), respectively. With increasing temperature from 700 to 1000 °C, the ratio of the
63 intensity of the D to the G band (I_D/I_G) decreased from 1.14 to 0.89, indicating increasing graphitization.
64 The I_D/I_G value is often used as a measure of defect density in graphite.^{19,20} In the case of CoNOCs, the
65 I_D/I_G maintained at high values, suggesting the presence of significant structural defects presumably
66 due to the presence of N and O dopants. It was suggested that these defects could promote the HER
67 electroactivity because more catalytic sites are exposed.²¹ The PXRD pattern of CoNOC-900 before
68 acid etching showed three sharp peaks at 44.2, 51.5, and 75.6° (Fig. 1e), which are representing the
69 characteristic (111), (200), and (220) reflections of cubic Co,²² respectively. Additionally, the product
70 showed two small peaks at 41.5 and 47.3° probably due to the formation of CoO. It can be assumed that
71 during the acid treatment cobalt compounds which are easier accessible, e.g. not fully encapsulated in
72 the carbon matrix will be primarily etched out. Indeed the diffraction peaks attributed to metal species
73 are not detectable for CoNOC-900 and CoNOC-1000, but still visible for CoNOC-700 and CoNOC-
74 800, however with much lower intensity. Inductively coupled plasma mass spectrometry (ICP/MS) and
75 elemental analysis (EA) measurements indicate that 2.45, 1.13, 0.46, and 0.17 wt% of Co, along with
76 3.45, 2.08, 1.35, and 1.17 wt% of N remained in CoNOC-700, CoNOC-800, CoNOC-900, and
77 CoNOC-1000 (Table S1), respectively.

78
79
80
81



82

83

84

Fig. 1 Preparation and characterization of CoNOCs. (a,b) Synthetic schemes, (c) FT-IR, (d) Raman, and (e) PXRD spectra of the CoNOCs.

85

86

87 As shown by the scanning electron microscopy (SEM) images (Figs. 2a, S1), the agglomerates of

88 CoNOCs consist of particles with diameters of 50-100 nm. With increasing pyrolysis temperature, it

89 appears that the nanoparticles tend to form sheet-like structures owing to the increased graphitization.

90 Transmission electron microscopy (TEM) measurements for CoNOC-900 (Fig. 2b), furthermore show

91 the formation of small Co nanoparticles (CoNPs) with an average diameter of *ca.* 10 nm within the

92 porous carbon structure. Diffused ring patterns were observed from the selected-area electron

93 diffraction (SAED) analysis of one CoNP which determined the polycrystalline nature of the CoNPs (Fig.

94 2c).²³ Sensitive high angle annular dark field (HAADF) scanning transmission electron microscopy

95 (STEM) imaging combined with energy-dispersive X-ray spectroscopy (EDX) elemental mapping

96 further proves the presence and uniform distribution of N and Co within the carbon matrix (Fig. 2d-f

97 and Figs. S2-4). HAADF STEM and atomic-scale high-resolution TEM (HRTEM) characterizations

98 furthermore show that the CoNPs are tightly encapsulated by graphitic carbon (Fig. 2e,h,i). As can be

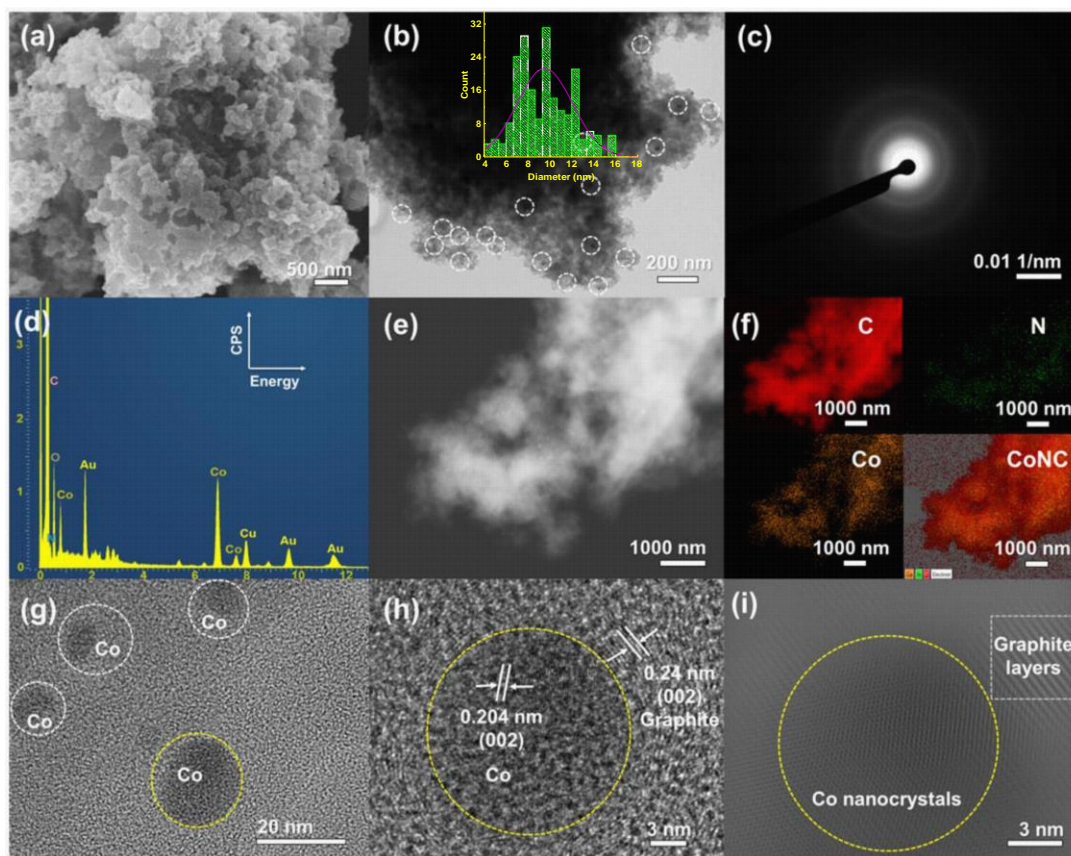
99 seen in the Fig. 2g-i, two lattice fringes are measured to be ~ 0.20 and ~ 0.24 nm, which are consistent

100 with the (111) and (002) lattice parameters for the cubic bulk Co nanocrystal cores and graphitic shells

101 (Fig. S5),²⁴ respectively. Note that the graphitic shells exhibit 5-15 layers. Before acid washing, a larger

102 population of CoNPs with an average diameter of *ca.* 10 nm can be seen from HRTEM analysis (Fig.

103 S6), which implies that the remaining CoNPs after acid washing are well encapsulated in CoNOCs.



104
 105 **Fig. 2 Characterization of CoNOCs.** (a) SEM, (b) TEM, (c) SEAD, (d) EDX, (e) STEM images as
 106 well as (f) C, N, Co, and their composite (CoNC) mapping, (g,h) HRTEM and (i) inverted fast Fourier
 107 transform (IFFT) contrast enhanced atomic resolution HRTEM images of CoNOC-900. Circled
 108 particles (b, g-i) show CoNPs (yellow circle shows the same particle in g,h,i), the square (i) graphitic
 109 layers. . The inset on Fig. 2b shows the size distribution of the CoNPs

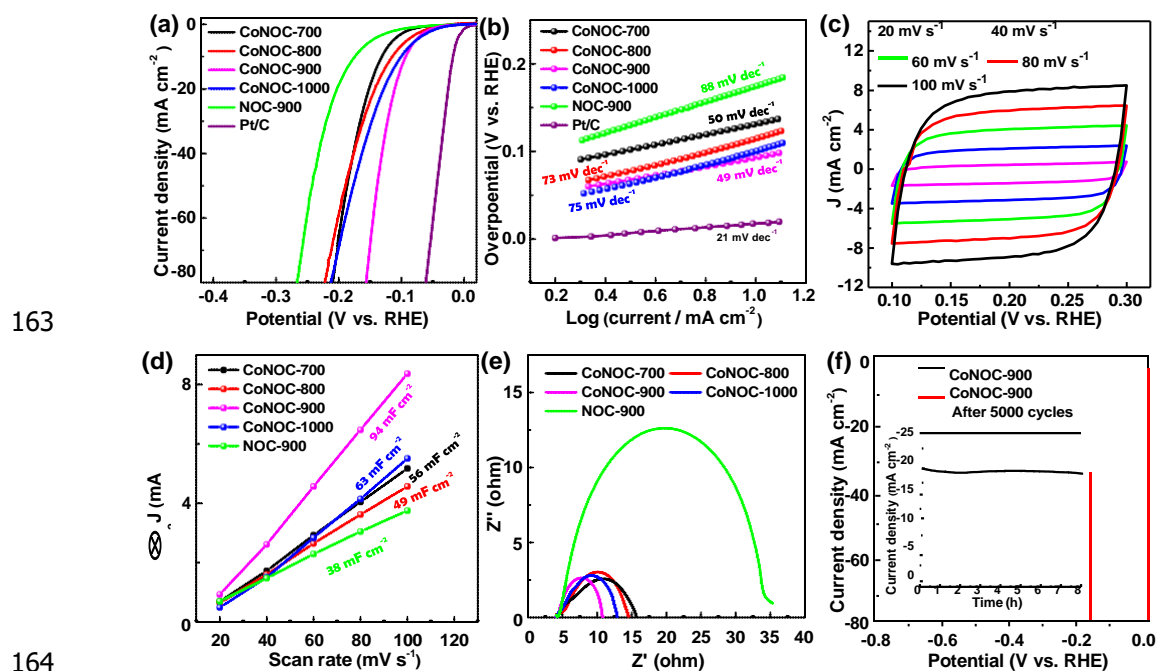
110

111 X-ray photoelectron spectroscopy (XPS) survey spectra confirm the presence of N, O, and C in the
 112 CoNOCs (Fig. S7). However, the Co content measured by the surface sensitive XPS is much lower
 113 than obtained by ICP/MS measurements (Table S1), indicating again the encapsulation of the CoNPs
 114 by carbon layers. In contrast, the Co2p core-level XPS spectrum of CoNOC-900 prepared without acid
 115 etching show much more intense peaks associated to metallic Co and CoO (Fig. S8),^{25,26} Among the
 116 samples, CoNOC-700 exhibits the highest N content with up to 3.65 wt%, as determined by XPS. The
 117 N1s core-level XPS spectra of all CoNOCs can be deconvoluted into four individual peaks that are
 118 assigned to pyridinic N (~398.4 eV), pyrrolic N (~400.1 eV), graphitic N (~401.2 eV), and oxidized N
 119 (~402.9 eV),²⁷ respectively (Fig. S9a). With increasing pyrolysis temperature the fraction of pyridinic
 120 N and pyrrolic N in comparison to the graphitic N decreased. Notably, CoNOC-900 showed a higher
 121 fraction of pyridinic and graphitic N compared to NOC-900, i.e. prepared in absence of Co, further
 122 supporting that the CoNPs promote graphitization. Such pyridinic and graphitic nitrogen-species are
 123 believed to be beneficial for the electrocatalytic activity according to previous studies.²⁸ The samples

124 also showed a high amount of oxygen in the carbon lattice (7.2-12.4 wt%), as determined by XPS.
125 Their O1s core-level XPS spectra can be deconvoluted into three peaks at ~531.5, ~532.6, and ~533.6
126 eV (Fig. S9b), which are assigned to the C-O, N⁺-O⁻, and C=O bonds of adsorbed water or phenolic
127 hydroxyl groups, oxidized graphitic N, and carbonyl units, respectively.^{29,30} According to the N₂
128 adsorption isotherms (Fig. S10), the Brunauer-Emmett-Teller (BET) surface areas of CoNOC-700,
129 CoNOC-800, CoNOC-900, and CoNOC-1000 are 207, 329, 486, and 394 m² g⁻¹ (Table S2),
130 respectively. CoNOC-900 and CoNOC-1000 exhibited similar surface areas (486 vs. 458 m² g⁻¹). The pore
131 size distribution (PSD) analyses showed that the pore sizes of all materials are mainly smaller than 2
132 nm (Fig. S11), with micropores contributed >80% to the overall surface area except for CoNOC-1000
133 due to the highest degree of graphitization. Note that CoNOC-900 and CoNOC-1000 showed an
134 additional outer surface area originating from the interparticular voids, as evidenced by the steep
135 increase of N₂ uptake at relative pressure (p/p₀) above 0.9. Such porosity found on CoNOCs can
136 promote catalytic site exposure and electron transfer, which are favorable for electrocatalysis.³¹

137 **HER performance of CoNOCs.** As shown in Fig. 3a, already N,O-dual doped NOC-900 is a good
138 HER catalyst, displaying a low overpotential of 175 mV (Table S3) at 10 mA cm⁻² i.e. a critical metric
139 in solar fuel production. However, also trace amounts of Pd residues (~0.05 wt%, as determined by ICP)
140 from polymer precursor synthesis can be responsible for the catalytic activity. With the encapsulation
141 of cobalt, CoNOCs exhibit an even better HER activity, as reflected by the large shift of the
142 polarization curves. CoNOC-700, CoNOC-800, CoNOC-900, and CoNOC-1000 show overpotentials
143 (at 10 mA cm⁻², η_{10}) of 132, 115, 93, and 102 mV and onset overpotentials (η_{onset}) of 72, 33, 22, and 23
144 mV (Table S3), respectively, showing that electrocatalysts prepared at 900 °C in presence of Co(acac)₂
145 gave the best HER activity (Figs. S12,13). The best η_{10} obtained on CoNOC-900 i.e. 93 mV compares
146 very well to the values obtained on many metal-containing HER carbon electrocatalysts (see detailed
147 comparisons in Table S4),^{7,32-37} and is also comparable to the best values recently reported on P-
148 Mo₂C@C nanowires (89 mV)³⁸ and CoP@BCN-1 nanotubes (87 mV).³⁹ The Tafel plots of the
149 polarization curves provide insight into the HER pathways on various catalysts (Fig. 3b). The
150 commercial Pt/C electrode exhibit a Tafel slope of 21 mV dec⁻¹, indicating that hydrogen is produced
151 *via* the rate-determining Heyrovsky step ($H^* + H^+ + e^- \rightarrow H_2$ or $H^* + H_2O + e^- \rightarrow H_2 + OH^-$), which is
152 consistent with the known mechanism of HER on Pt.⁴⁰ The NOC-900 catalyst showed a Tafel slope of
153 88 mV dec⁻¹, suggesting that an initial proton adsorption is the rate-determining step ($H^+ + e^- \rightarrow H^*$ or
154 $H_2O + e^- \rightarrow H^* + OH^-$) on the metal-free catalyst.⁴⁰ The Tafel analyses of the CoNOC catalysts finally
155 reveal Tafel slopes of 49-75 mV dec⁻¹, indicating that hydrogen is produced *via* the Volmer-Heyrovsky
156 mechanism i.e. the electrochemical desorption is the rate-determining step.⁴¹ On the basis of the Tafel
157 plots, the exchange current density of the catalysts was estimated to be 4.3×10^{-4} A cm⁻² (Table S3),
158 which is close to that of Pt/C (5.4×10^{-4} A cm⁻²).³⁸ The differences in HER electrocatalytic activities of
159 our CoNOC catalysts could be mainly attributed to the electrochemically active surface area (ECSA)
160 and electron transfer rate. Double-layer capacitance (C_{dl}) extracted from the capacitive current as a

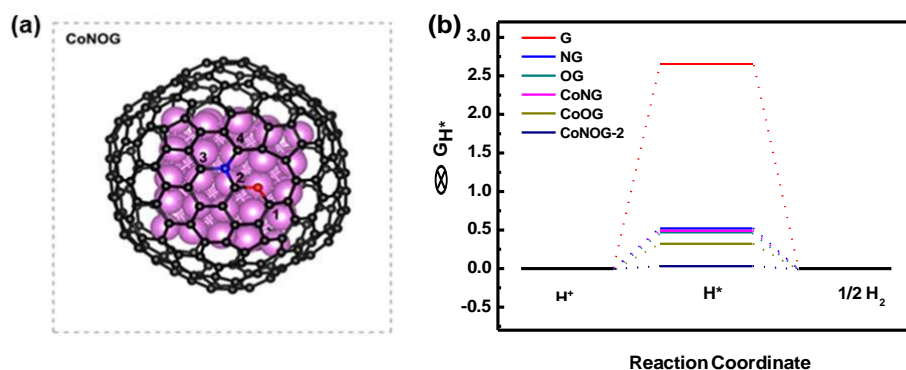
161 function of scan rate is generally used for the estimation of the effective ECSA of the solid/liquid
 162 interface, which can be calculated from cyclic voltammetry (CV) curves scanned at different rates.



164
 165 **Fig. 3 HER performance of CoNOCs.** (a) Polarization curves and (b) corresponding Tafel plots of
 166 CoNOC catalysts obtained in 0.5 M H₂SO₄ solution, along with NOC-900 and commercial Pt/C
 167 catalysts for comparison; (c) cyclic voltammograms (CV) of CoNOC-900 obtained with different rates
 168 from 20-100 mV s⁻¹ in a potential range of 0.1-0.3 V without faradaic processes; (d) capacitive current
 169 density as functions of scan rate and (e) electrochemical impedance Nyquist plots of for CoNOC
 170 catalysts, along with NOC-900 catalyst for comparison; (f) stability tests of CoNOC-900 catalyst upon
 171 5000 potential cycles, inset showing the time dependence of catalytic currents during electrolysis.

172
 173 As shown in Fig. 3c and Fig. S14, the CV curves of all the catalysts showed roughly rectangular shapes
 174 owing to the double-layer capacitance. CoNOC-900 showed the largest C_{dl} of 94 mF cm⁻² (Fig. 3d),
 175 compared to CoNOC-700 (56 mF cm⁻²), CoNOC-800 (49 mF cm⁻²), and CoNOC-1000 (63 mF cm⁻²).
 176 The C_{dl} obtained on CoNOC-900 is nearly 2.5 times higher than that of NOC-900 (94 vs. 38 mF cm⁻²),
 177 signifying the largest ECSA. Electrical impedance measurements showed the smallest semicircle in the
 178 Nyquist plots (Fig. 3e), indicating the lowest charge-transfer resistance. To test the durability of the
 179 catalysts in an acidic environment, long-term potential cycling was performed in a 0.5 M H₂SO₄
 180 solution by continuous CV scanning at a rate of 50 mV s⁻¹ for 5000 cycles. As shown in Fig. 3f and Fig.
 181 S15, although the polarization curves of the CoNOC-700, CoNOC-800, and CoNOC-1000 catalysts
 182 showed a slight decay, CoNOC-900 shows a very stable performance, with a negligible loss of current
 183 density of 20 mA cm⁻² over 8 hours (Fig. 3f, inset). Further post mortem characterization including
 184 SEM and ICP/MS analyses of catalyst upon 5000 cycling indicated negligible changes in compositions
 185 and morphologies (Fig. S16).

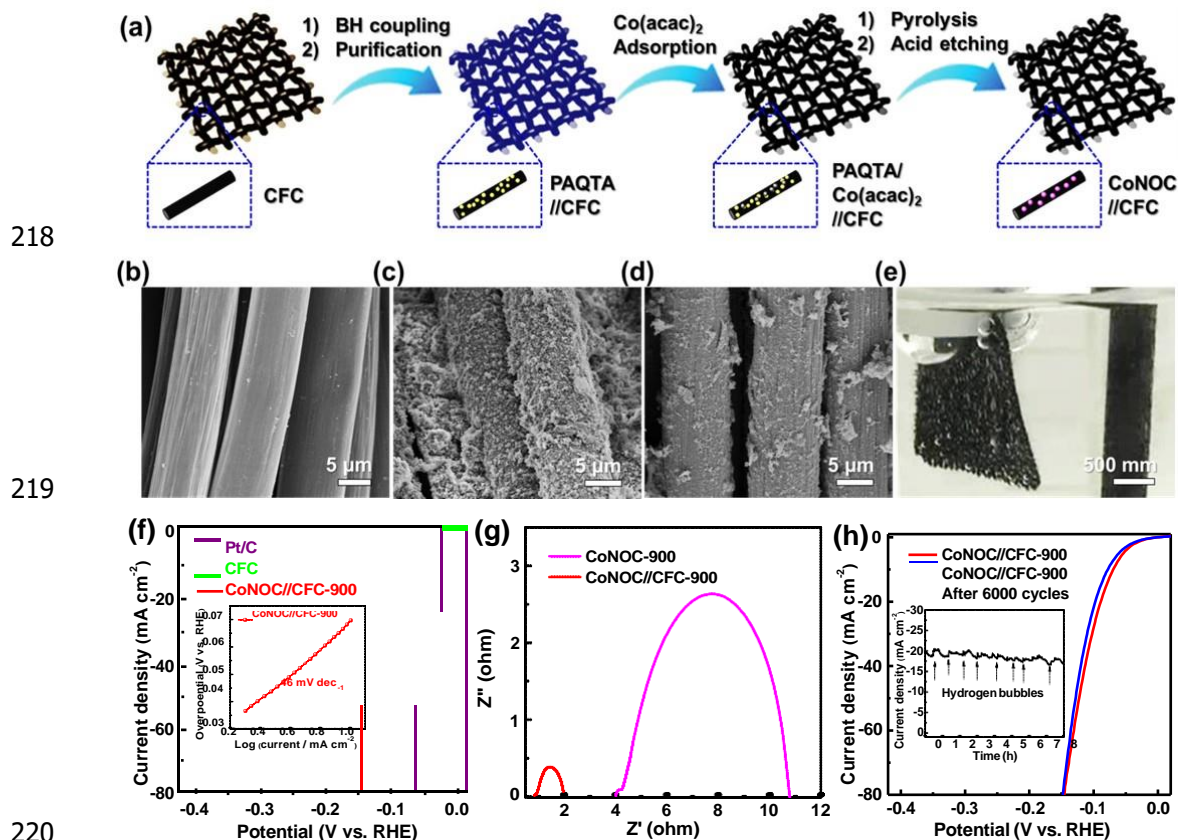
186 **Density functional theory (DFT) calculations.** The adsorption free energy of H^* (ΔG_{H^*}) is one of the
 187 most important benchmarks determining the HER activity for electrocatalysts.^{42,43} A smaller ΔG_{H^*}
 188 value usually yield a better HER activity and an optimal HER catalyst should have a ΔG_{H^*} value close
 189 to zero to compromise the reaction barriers of the adsorption and desorption steps. To explain the
 190 superior activity of our catalyst and the influence of the present heteroatoms and metal particles, ΔG_{H^*}
 191 values were calculated for various models including pure graphene (G), N-doped graphene (NG), O-
 192 doped graphene (OG), N-doped graphene encapsulated Co (CoNG), and O-doped graphene
 193 encapsulated Co (CoOG). Besides, also four possible H^* adsorption sites in N,O-dual doped graphene
 194 encapsulated Co were calculated (CoNOG-1, 2, 3, and 4). The optimized models are illustrated in Fig.
 195 4a and Figs. S17,18 and the specific ΔG_{H^*} values are shown in Table S4. According to the calculated
 196 ΔG_{H^*} diagram shown in Fig. 4b, the value of ΔG_{H^*} decreased strongly already after introduction of N
 197 and O dopants in the carbon layers. The combination of a Co metal core and a graphene shell can
 198 further decrease the value of ΔG_{H^*} . However, N,O-dual doped graphene encapsulated Co exhibits the
 199 lowest ΔG_{H^*} value among the various models, especially for CoNOG-2 with a value very close to zero.
 200 The results show that the introduction of Co, N, and O can remarkably reduce the ΔG_{H^*} , explaining the
 201 superior HER activity.



202
 203 **Fig. 4 DFT calculations.** (a) Optimized structure of N,O-dual doped graphene encapsulated CoNPs
 204 and four possible H^* adsorption sites; (b) calculated ΔG_{H^*} diagram of various models.

205 **HER performance of CoNOC//CFCs.** The use of a polymeric precursor give rise for the fabrication
 206 of self-standing membrane-type electrodes by growing the polymer networks on carbon fiber cloth
 207 (CFC). As illustrated in Fig. 5a, adding the CFC within the solution of the BH reaction afforded a
 208 uniform deposition of PAQTA on the surface of carbon fibers as seen by SEM (Fig. 5b-d). Co
 209 impregnation, pyrolysis and acid etching was carried out like the optimized procedure for the bulk
 210 materials described before to yield CFC-supported electrodes i.e. CoNOC//CFC-x. As shown in Fig. 5e
 211 and the supporting videos, CoNOC//CFC-900 produced hydrogen even faster than CoNOC-900. Indeed,
 212 based on the polarization curve measurements, CoNOC//CFC-900 is much more active than CoNOC-
 213 900, displaying η_{10} and η_{onset} of 69 and 15 mV, respectively (Fig. 5f). Electrical impedance
 214 measurements also indicated a much lower charge-transfer resistance (Fig. 5g). The Tafel slope and
 215 exchange current density of CoNOC//CFC-900 were calculated to be 46 mV dec^{-1} and $1.1 \times 10^{-4} \text{ A cm}^{-2}$

216 ², respectively. The promoted electrocatalytic activity can be explained by a very low threshold of
 217 conductivity resulting from the binder-free assembly of the membrane-type electrode.



221 **Fig. 5** HER performance of CoNOC//CFCs. (a) Schematic illustration of the synthesis of self-
 222 supporting membrane-type CoNOC//CFC electrode, (b) pristine CFC, (c) CFC after PAQTA
 223 deposition, (d) PAQTA-deposited CFC upon pyrolysis and acid etching, (e) visible hydrogen
 224 production upon applying a 20 mV voltage on CoNOC//CFC-900 for 30 seconds, (f) polarization
 225 curves and Tafel plots, (g) Nyquist plots (tested at 5 mV AC potential from 10 kHz to 0.1 Hz), and (h)
 226 cyclability of CoNOC//CFC-900.

228 Although interfered by the large amount of bubbles during the HER, CoNOC//CFC-900 still showed a
 229 quite stable current density ca. $19.5 \pm 0.5 \text{ mA cm}^{-2}$ (only $\sim 2.5\%$ variations) over 8 hours (Fig. 5h),
 230 inset), showing an excellent catalytic durability. Overall, the obtained HER activities e.g. η_{10} (69 mV)
 231 and Tafel slope (46 mV dec^{-1}) outperforms most recent carbon-based HER catalysts (see detailed
 232 comparisons in Table S4).⁴⁴⁻⁵⁰ As an important feature, the here shown membrane-type electrode could
 233 be readily scaled-up owing to the simple *in-situ* deposition, facile pyrolysis, and tailorable CFCs
 234 involved. Using such a scaled-up electrode of CoNOC//CFC-900 (1.3 cm \times 1.5 cm in size, 50 μm
 235 in thickness, and 1.365 mg of active substance), a proof-of-concept demonstration for efficient water
 236 splitting is displayed in a supporting video. The electrode roughly produced 4 mL of hydrogen per

237 minute in a rate of $2.93 \text{ L g}^{-1} \text{ min}^{-1}$ upon applying a 20 mV voltage, making this material promising for
238 environment-friendly hydrogen-production.

239 In summary, we have developed a simple, low-cost, and efficient route to N,O-dual doped carbons
240 encapsulated cobalt nanoparticles by pyrolysis of an anthraquinonylamine and triphenylamine-based
241 conjugated microporous polymer in presence of cobalt(II) acetylacetonate. The resulting porous
242 carbons with a trace amount of CoNPs exhibited remarkable activity and durability for the hydrogen
243 evolution reaction (HER), which outperforms most of the non-noble metal-based catalysts in acidic
244 solutions. The density functional theory calculations indicated that N,O-dual doping and Co
245 encapsulation significantly decreased the hydrogen adsorption free energy on the surface of the
246 catalysts explaining the superior HER activity. Furthermore, growth of the polymeric pre-catalyst on
247 carbon fiber cloth and subsequent pyrolysis afforded binder-free HER electrode, which was even more
248 active for HER. Owing to the scalability and versatility of the here shown approach, it could be further
249 applied for the rational design of high-performance electrocatalysts for water splitting, batteries, and
250 other electrochemical devices.

251 **Methods**

252 **Synthesis of CoNOCs.** The precursor PAQTA was synthesized using Buchwald-Hartwig (BH)
253 coupling method.¹⁸ To synthesize the CoNOC catalysts, $\text{Co}(\text{acac})_2$ was impregnated in PAQTA
254 pyrolyzed and washed with H_2SO_4 . Specifically, 100 mg PAQTA and 771 mg $\text{Co}(\text{acac})_2$ were
255 suspended in 30 mL toluene. After stirring the dispersion for 6 h at 80°C , the metal-impregnated
256 CoNOCs were collected by filtration. The resulting powders were pyrolyzed at a temperature of 700,
257 800, 900 and 1000°C , respectively, for 3 h in a N_2 atmosphere, then etched in 0.5 M H_2SO_4 for 24 h (3
258 $\times 8$ h), washed with a plenty of water (3×200 mL) and then dried at 60°C .

259 **Preparation of CoNOC and CoNOC//CFC electrodes.** To prepare the CoNOC electrodes using a
260 binder, 5 mg of catalyst was dispersed in a 50 μL 5 wt% Nafion solution (Sigma Aldrich) and 200 μL
261 ethanol, and then sonicated to obtain a homogeneous ink. A certain amount of catalyst ink was drop-
262 casted on a polished glassy carbon rotating disk electrode (RDE, Pine, USA, diameter: 5 mm;
263 geometric area: 0.196 cm^2 ; catalyst loading: $\sim 0.3 \text{ mg cm}^{-2}$) and dried in 50°C oven, affording the
264 CoNOC electrodes. The BH reaction yielded PAQTA-deposited in carbon fibers, providing a host for
265 $\text{Co}(\text{acac})_2$ adsorption. Further pyrolysis and acid etching afforded CoNOC//CFC electrodes.
266 Specifically, a Schlenk tube was charged with carbon fiber cloth (CFC, thickness: 0.36 mm, resistance:
267 $< 1.2 \text{ m}\Omega/\text{cm}^2$, size: $1.0 \text{ cm} \times 1.5 \text{ cm}$), DAQ (180 mg, 0.75 mmol), TA (245 mg, 0.5 mmol), XPhos
268 (21.5 mg, 0.045 mmol), a small amount of $\text{Pd}(\text{dba})_2$ (17 mg, 0.03 mmol), and NaOtBu (192 mg, 2 mmol)
269 and placed in N_2 atmosphere. Toluene (50 mL) was added and the reaction was heated to 110°C under
270 stirring for 24 h, then the CFC was removed and washed with DMF, hot MQ water, and CHCl_3 (24 h
271 each, 3×200 mL) and then dried in a vacuum oven (50°C) for 72 h. The CFC deposited with PAQTA
272 and 771 mg $\text{Co}(\text{acac})_2$ were suspended in 30 mL toluene. After stirring the dispersion for 6 h at 80°C ,
273 the metal-impregnated CFC was collected by filtration and pyrolyzed at 900°C for 3 h in a N_2

274 atmosphere. The product was etched in 0.5 M H₂SO₄ for 24 h (3 × 8 h), washed with water (3 × 200
275 mL) and then dried at 60 °C, affording membrane-type electrode CoNOC//CFC-900.

276 **DFT calculations.** DFT calculations were carried out using the Vienna Ab Initio Simulation Package
277 (VASP), with supplied Projector Augmented Wave (PAW) potentials for core electrons. The
278 generalized gradient approximation (GGA) of Perdew–Becke–Ernzerhof (PBE) is used for the
279 exchange–correlation functional. A graphitic carbon cage C240 encapsulated 55 metal atoms was used
280 as the model of graphene encapsulated alloys, which performed well in previous study.^{6,12} The cut-off
281 energies for plane waves is 400 eV, providing a convergence of 10⁻⁴ eV in total energy and 0.05 eV/Å
282 in Hellmann Feynman force on each atom. The hydrogen binding energy ΔE_H was calculated by $\Delta E_H = E_{\text{slab}} - E_{\text{slab}} - E_{\text{H}_2} - E_{\text{H}}$
283 according to previous work, where, ΔE_H , E_{slab} , E_{H_2} and E_{H} are the total energy of graphene-encapsulated metal,
284 the hydrogen binding energy, ΔZPE , ΔS and U are the zero point energy changes and entropy
285 changes, respectively.

284
285
286

287 **Sample characterization.** FT-IR spectra were taken on a Nicolet 670 spectrometer. Raman spectra
288 were recorded on a Renishaw InVia Reflex spectrometer. PXRD patterns were obtained on a Bruker
289 D8 Advance diffractometer (40 kV, 30 Ma) using Cu K α radiation ($2\theta = 2-90^\circ$). XPS were obtained on
290 a Thermo Fisher Scientific ESCALAB 250Xi spectrometer. TGA was carried out on a Mettler Toledo
291 TGA 1 instrument in air in the temperature range 30-1000 °C (heating rate 10 °C/min). SEM images
292 were obtained on a HITACHI S-4800 microscopy. The size distributions and microstructure were
293 analyzed by TEM, HRTEM and SAED on a JEOL-3000F at 300kV. The histogram of the size
294 deviation was generated from a statistical measurement on 200 particles. SAED analysis was
295 performed on JEOL-3000F at 300kV and the camera length was 255.8 mm. HAADF-STEM and XEDS
296 elemental mapping were performed on a JEOL JEM-2100. All specimens were prepared by dispersing
297 samples into ethanol and then drop-casted onto holy carbon supported Au grids. The metal
298 compositions were analyzed using a Leeman Labs Prodigy ICP/MS along with XPS, XEDS, and
299 PXRD. N₂ adsorption/desorption measurements at 77.4 were performed after degassing the samples
300 under high vacuum at 120 °C for 15 hours using a Micro ASAP2046 machine.

301 **Electrochemical measurements.** All the electrochemical measurements were performed in a three-
302 electrode system on an electrochemical workstation (Gamry Interface 1100E, USA) in 0.5 M H₂SO₄ at
303 room temperature. All tests were performed with iR compensation. For non-supported catalyst tests, the
304 synthesized catalyst dispersed onto a glass carbon RDE were used as a working electrode, a saturated
305 calomel electrode (SCE) was used as the reference electrode, and a graphite rod was served as the
306 counter electrode. Linear sweep voltammetry (LSV) scans with a rate of 5 mV s⁻¹ was conducted after
307 purged the electrolyte solutions for 30 min ensuring the complete elimination of dissolved oxygen.
308 During the measurements, the headspace of the electrochemical cell was continuously purged with N₂.
309 Electrochemical impedance spectroscopy (EIS) Nyquist plots were obtained by carrying out the
310 measurements in the same configuration at $\eta = 0.15$ V from 10⁵-0.1 Hz with an AC voltage of 5 mV.

311 The stability testing of the catalysts were examined by continuously cycling the potential between +0.1
312 and -0.5 V vs. RHE at a scan rate of 50 mV/s while the time-dependent stability were operated at a
313 constant current density of 20 mA cm⁻². For self-supporting catalyst test, the membrane-type catalyst
314 was directly used as the working electrode. The LSV, EIS, and stability measurements were carried out
315 as same as that procedure applied for non-supported catalyst tests. All of the potentials were calculated
316 according to $E_{\text{RHE}} = 0.242 + 0.059 \text{ pH}$. The Tafel slope was calculated from polarization curves on the
317 basis of the Tafel equation: $\eta = a + b \log j$, where η is the overpotential (mV), b is the Tafel slope, j is
318 the current density (mA cm⁻²). Moreover, the exchange current density (j_0) was obtained by
319 extrapolation of Tafel plots ($\eta = 0, j_0 = 10^{(-a/b)}$). Double-layer capacitance (C_{dl}) was obtained by cyclic
320 voltammetry measurements in the potential range of 0.1 to 0.3 V vs. RHE with scan rates from 20 to
321 100 mV s⁻¹. The capacitive currents of $\Delta J_{\text{Ja-Jc}}/2$ at 0.2 V vs. RHE were plotted against the scan rates.
322 The slope of the curves was the double-layer capacitance.

323 **Data availability.** The data that support this paper and other findings of this study are available from
324 the corresponding author upon reasonable request.

325 References

- 326 1. Lu, Q. P. et al. 2D Transition-metal-dichalcogenide-nanosheet-based composites for photocatalytic
327 and electrocatalytic hydrogen evolution reactions. *Adv. Mater.* **28**, 1917-1933 (2016).
- 328 2. Hinnemann, B. et al. Biomimetic hydrogen evolution: MoS₂ nanoparticles as catalyst for hydrogen
329 evolution. *J. Am. Chem. Soc.* **127**, 5308-5309 (2005).
- 330 3. Chen, W. F. et al. Hydrogen-evolution catalysts based on non-noble metal nickel-molybdenum nitride
331 nanosheets. *Angew. Chem. Int. Ed.* **51**, 6131-6135 (2012).
- 332 4. Cao, B. F. et al. Mixed close-packed cobalt molybdenum nitrides as non-noble metal electrocatalysts for
333 the hydrogen evolution reaction. *J. Am. Chem. Soc.* **135**, 19186-19192 (2013).
- 334 5. Le, G. A. et al. From hydrogenases to noble metal-free catalytic nanomaterials for H₂ production
335 and uptake. *Science* **326**, 1384-1387 (2009).
- 336 6. Deng, J., Ren, P. J., Deng, D. H. & Bao, X. H. Enhanced electron penetration through an ultrathin
337 graphene layer for highly efficient catalysis of the hydrogen evolution reaction. *Angew. Chem. Int.*
338 *Edit.* **54**, 2100-2104 (2015).
- 339 7. Deng, J. et al. Highly active and durable non-precious-metal catalysts encapsulated in carbon
340 nanotubes for hydrogen evolution reaction. *Energy Environ. Sci.* **7**, 1919-1923 (2014).
- 341 8. Tavakkoli, M. et al. Single-shell carbon-encapsulated iron nanoparticles: synthesis and high
342 electrocatalytic activity for hydrogen evolution reaction. *Angew. Chem. Int. Edit.* **54**, 4535-4538
343 (2015).
- 344 9. Wang, J. et al. Non-noble metal-based carbon composites in hydrogen evolution reaction:
345 fundamentals to applications. *Adv. Mater.* **29**, 1605838 (2017).
- 346 10. Chung, D. Y. et al. Large-scale synthesis of carbon-shell-coated FeP nanoparticles for robust
347 hydrogen evolution reaction electrocatalyst. *J. Am. Chem. Soc.* **139**, 6669-6674 (2017).

- 348 11. Wang, J. H. et al. Recent progress in cobalt-based heterogeneous catalysts for electrochemical
349 water splitting. *Adv. Mater.* **28**, 215-230 (2016).
- 350 12. Su, J. W. et al. Ruthenium-cobalt nanoalloys encapsulated in nitrogen-doped graphene as active
351 electrocatalysts for producing hydrogen in alkaline media. *Nat. Commun.* **8**, 14969 (2017).
- 352 13. Zhang, L. L., Xiao, J., Wang, H. Y. & Shao, M. H. Carbon-based electrocatalysts for hydrogen and
353 oxygen evolution reactions. *ACS Catal.* **7**, 7855-7865 (2017).
- 354 14. Lu, C. B. et al. Molybdenum carbide-embedded nitrogen-doped porous carbon nanosheets as
355 electrocatalysts for water splitting in alkaline media. *ACS Nano* **11**, 3933-3942 (2017).
- 356 15. Qu, K. G. et al. Polydopamine-inspired, dual heteroatom-doped carbon nanotubes for highly
357 efficient overall water splitting. *Adv. Energy Mater.* **7**, 1602068 (2017).
- 358 16. Chaoui, N. et al. Trends and challenges for microporous polymers. *Chem. Soc. Rev.* **46**, 3302-3321
359 (2017).
- 360 17. Xu, F., Wu, D. C., Fu, R. W. & Wei, B. Q. Design and preparation of porous carbons from
361 conjugated polymer precursors. *Nano Today* **20**, 629-656 (2017).
- 362 18. Liao, Y. Z., Wang, H. G., Zhu, M. F. & Thomas, A. Efficient supercapacitor energy storage using
363 conjugated microporous polymer networks synthesized from Buchwald-Hartwig coupling. *Adv.*
364 *Mater.* **1705710** (2018).
- 365 19. Zou, X. X. et al. Cobalt-embedded nitrogen-rich carbon nanotubes efficiently catalyze hydrogen
366 evolution reaction at all pH values. *Angew. Chem.* **126**, 4461-4465 (2014).
- 367 20. Yang, H. B. et al. Identification of catalytic sites for oxygen reduction and oxygen evolution in N-
368 doped graphene materials: development of highly efficient metal-free bifunctional electrocatalysts.
369 *Sci. Adv.* **2**, e1501122 (2016).
- 370 21. Yang, Y. et al. Tuning electronic structures of nonprecious ternary alloys encapsulated in graphene
371 layers for optimizing overall water splitting activity. *ACS Catal.* **7**, 469-479 (2017).
- 372 22. Ma, J.-L., Meng, F.-L., Xu, D. & Zhang, X.-B. Co-embedded N-doped carbon fibers as highly
373 efficient and binder free cathode for Na-O₂ batteries. *Energy Storage Mater.* **6**, 1-8 (2017).
- 374 23. Hou, B. et al. Structure and band edge energy of highly luminescent CdSe_{1-x}Tex alloyed quantum
375 dots. *J. Phys. Chem. C* **117**, 6814-6820 (2013).
- 376 24. Zeng, M. et al. Metallic cobalt nanoparticles encapsulated in nitrogen-enriched graphene shells: its
377 bifunctional electrocatalysis and application in zinc-air batteries. *Adv. Funct. Mater.* **26**, 4397-4404
378 (2016).
- 379 25. Wang, J. et al. CoO_x-carbon nanotubes hybrids integrated on carbon cloth as a new generation of
380 3D porous hydrogen evolution promoters. *J. Mater. Chem. A* **5**, 10510-10516 (2017).
- 381 26. Zhang, P. et al. 3D hierarchical Co/CoO-graphene-carbonized melamine foam as a superior
382 cathode toward long-life lithium oxygen batteries. *Adv. Funct. Mater.* **26**, 1354-1364 (2016).
- 383 27. Zhang, J. T. & Dai, L. M. Nitrogen, phosphorus, and fluorine tri-doped graphene as a
384 multifunctional catalyst for self-powered electrochemical water splitting. *Angew. Chem. Int. Ed.*
385 **55**, 13296-13300 (2016).

- 386 28. Li, S. et al. 2D porous carbons prepared from layered organic-inorganic hybrids and their use as
387 oxygen-reduction electrocatalysts. *Adv. Mater.* **29**, 1700707 (2017).
- 388 29. Hulicova-Jurcakova, D., Seredych, M., Lu, G. Q. & Bandosz, T. J. Combined effect of nitrogen-
389 and oxygen-containing functional groups of microporous activated carbon on its electrochemical
390 performance in supercapacitors. *Adv. Funct. Mater.* **19**, 438-447 (2009).
- 391 30. Guedidi, H. et al. The effects of the surface oxidation of activated carbon, the solution pH and the
392 temperature on adsorption of ibuprofen. *Carbon* **54**, 432-443 (2013).
- 393 31. Liang, H.-W. et al. Mesoporous metal-nitrogen-doped carbon electrocatalysts for highly efficient
394 oxygen reduction reaction. *J. Am. Chem. Soc.* **135**, 16002-16005 (2013).
- 395 32. Liu, Y. P. et al. Coupling Mo₂C with nitrogen-rich nanocarbon leads to efficient hydrogen-
396 evolution electrocatalytic sites. *Angew. Chem. Int. Ed.* **54**, 10752-10757 (2015).
- 397 33. Yang, J. et al. Porous molybdenum phosphide nano-octahedrons derived from confined
398 phosphorization in UIO-66 for efficient hydrogen evolution. *Angew. Chem.* **128**, 13046-13050
399 (2016).
- 400 34. Wang, Z.-L. et al. C and N hybrid coordination derived Co-C-N complex as a highly efficient
401 electrocatalyst for hydrogen evolution reaction. *J. Am. Chem. Soc.* **137**, 15070-15073 (2015).
- 402 35. Liang, H. W. et al. Molecular metal-N_x centres in porous carbon for electrocatalytic hydrogen
403 evolution. *Nat. Commun.* **6**, 7992 (2015).
- 404 36. Han, Q. et al. Mesh-on-mesh graphitic-C₃N₄@graphene for highly efficient hydrogen evolution.
405 *Adv. Funct. Mater.* **27**, 1606352 (2017).
- 406 37. Qu, K. G. et al. Promotion of electrocatalytic hydrogen evolution reaction on nitrogen-doped
407 carbon nanosheets with secondary heteroatoms. *ACS Nano* **11**, 7293-7300 (2017).
- 408 38. Shi, Z. P. et al. Phosphorus-Mo₂C@carbon nanowires toward efficient electrochemical hydrogen
409 evolution: composition, structural and electronic regulation. *Energy Environ. Sci.* **2017**, **10**, 1262-
410 1271.
- 411 39. Tabassum, H. et al. Metal-organic frameworks derived cobalt phosphide architecture encapsulated
412 into B/N Co-doped graphene nanotubes for all pH value electrochemical hydrogen evolution. *Adv.*
413 *Energy Mater.* **7**, 1601671 (2017).
- 414 40. Conway, B. E. & Tilak, B. V. Interfacial processes involving electrocatalytic evolution and
415 oxidation of H₂, and the role of chemisorbed H. *Electrochim. Acta* **47**, 3571-3594 (2002).
- 416 41. Deng, D. H. et al. Catalysis with two-dimensional materials and their heterostructures. *Nat.*
417 *Nanotech.* **11**, 218-230 (2016).
- 418 42. Jiao, Y., Zheng, Y., Davey, K. & Qiao, S.-Z. Activity origin and catalyst design principles for
419 electrocatalytic hydrogen evolution on heteroatom-doped graphene. *Nat. Energy* **1**, 16130 (2016).
- 420 43. Yang, Y. et al. Non-precious alloy encapsulated in nitrogen-doped graphene layers derived from
421 MOFs as an active and durable hydrogen evolution reaction catalyst. *Energy Environ. Sci.* **8**, 3563-
422 3571 (2015).

- 423 44. Wang, X.-D. et al. Novel porous molybdenum tungsten phosphide hybrid nanosheets on carbon
424 cloth for efficient hydrogen evolution. *Energy Environ. Sci.* **9**, 1468-1475 (2016).
- 425 45. Xiang, Z. C. et al. MoS₂ nanosheets array on carbon cloth as a 3D electrode for highly efficient
426 electrochemical hydrogen evolution. *Carbon* **98**, 84-89 (2016).
- 427 46. Huang, X. L. et al. Activating basal planes and S-terminated edges of MoS₂ toward more efficient
428 hydrogen evolution. *Adv. Funct. Mater.* **27**, 1604943 (2017).
- 429 47. Yan, X.-Y. et al. Self-supported rectangular CoP nanosheet arrays grown on a carbon cloth as an
430 efficient electrocatalyst for the hydrogen evolution reaction over a variety of pH values. *New J.*
431 *Chem.* **41**, 2436-2442 (2017).
- 432 48. Zhang, Y. Q. et al. Ultrafine metal nanoparticles/N-doped porous carbon hybrids coated on carbon
433 fibers as flexible and binder-free water splitting catalysts. *Adv. Energy Mater.* **7**, 1700220 (2017).
- 434 49. Yan, J. J. et al. MoSe₂ nanosheets grown on polydopamine-derived porous fibers: a high-
435 performance catalyst for hydrogen evolution reaction. *Adv. Mater. Interfaces* **4**, 1600825 (2017).
- 436 50. Ren, B. W. et al. Novel porous tungsten carbide hybrid nanowires on carbon cloth for high-
437 performance hydrogen evolution. *J. Mater. Chem. A* **5**, 13196-13203 (2017).

438 **Acknowledgments**

439 This work was supported by the National Natural Science Foundation of China (51673039), the
440 Shanghai Pujiang Talent Program (16PJ1400300), the Shanghai Key Fundamental Project
441 (16JC1400700/01) and the Fundamental Research Funds for the Central Universities (16D110618). We
442 furthermore acknowledge the support from the Sino-German Center for Research Promotion (GZ879).

443 **Author contributions**

444 Y.L. proposed the idea behind the research and supervised the project. H.W. and B.H. performed the
445 synthesis, characterization and measurements. Y.Y. carried out the model construction and DFT
446 calculations. All authors co-wrote the paper, discussed the results and commented on the manuscript.

447 **Competing interests**

448 The authors declare no competing financial interests.

449 **Additional information**

450 **Supplementary information.** Tables for elemental composition, porosity, catalytic activity summaries
451 and comparisons, SEM, TEM, HRTEM and STEM images, element mapping, XPS spectra, nitrogen
452 adsorption/desorption isotherms, pore size distribution, CV curves, electrocatalytic durability tests, and
453 DFT calculations. This material is available free of charge *via* the Internet at www.nature.com.

454
455
456
457